A comprehensive analysis of hierarchical porous carbons using a dualshape 2D-NLDFT model with adjustable slit-cylinder pore shape boundary

Jacek Jagiello, Jimena Castro-Gutiérrez, Rafael Luan Sehn Canevesi, Alain Celzard, Vanessa Fierro

A comprehensive analysis of hierarchical porous carbons using a dual-shape 2D-NLDFT model with adjustable slit-cylinder pore shape boundary

Jacek Jagiello[a*], Jimena Castro-Gutiérrez[b], Rafael Luan Sehn Canevesi[b], Alain Celzard[b], Vanessa Fierro[b*]

[a] Micromeritics Instrument Corporation, 4356 Communications Drive, Norcross, GA 30093, United States

[b] Université de Lorraine, CNRS, IJL, F-88000 Epinal, France

Keywords: NLDFT model, pore shape, slit-cylinder boundary, hierarchical porous carbons, pore size distribution

[a*]Corresponding author. Tel: +1 770 624 3379. E-mail: Jacek.Jagiello@micromeritics.com

[b*]Corresponding author. Tel: +33 (0)372 749 677. E-mail: Vanessa.Fierro@univ-lorraine.fr

Abstract

A thorough characterization of the textural properties of hierarchical porous carbons (HPCs) is of utmost importance as it provides information that aids in the selection of a suitable material for a given application and in understanding the phenomena observed once the material becomes part of a system. Gas adsorption-desorption isotherms coupled with the application of density functional theory (DFT) models to these isotherms are common tools for the textural characterization of HPCs, for which pore shape is an essential factor for the determination of pore size distributions (PSDs). By analyzing the experimental adsorption data of a series of CO_2-activated HPCs with a progressive development of porosity, it is shown that artifacts are found in the derived PSDs when a slit-cylinder pore shape boundary is fixed at 2 nm, which is the case for the original dual-shape non-local DFT (2D-NLDFT-HS) and the hybrid quenched solid DFT (QSDFT) models. This study presents a new dual-shape 2D-NLDFT-HS (DS-HS) model that, combined with the 2D-NLDFT-HS model for CO_2, provides the possibility of analyzing simultaneously N_2 and CO_2 adsorption-desorption isotherms and adjusting at the same time the limits for the assumed slit and cylindrical pore shapes. Using the DS-HS approach and adjusting the slit-cylinder boundary at 3 nm allowed eliminating PSDs artifacts. The interactive adjustment of the slit-cylindrical pore shape boundary of the DS-HS model represents a major advantage of this approach allowing for a comprehensive analysis of the adsorption data and a more accurate description of the textural properties of HPC materials.

1. Introduction

Hierarchical porous carbons (HPCs), *i.e.*, materials with pores of different widths (w) that can be classified as micro-, meso- and macropores ($w < 2$ nm, $2 < w < 50$ nm, and 50 nm $< w$, respectively),[1] have attracted the interest of the chemistry and engineering scientific community due to their versatility. Carbon precursors are abundant in nature and, depending on their origin and processing, the obtained HPCs can exhibit an interesting combination of characteristics that make them suitable for a wide range of applications like gas adsorption and separation,[2,3] wastewater treatment,[4] drug delivery and bioimaging,[5] catalysis,[6,7] energy storage in batteries and supercapacitors,[8–10] hydrogen storage,[11] among others.[12,13] For instance, it has been shown that a hierarchical porous carbon (HPC) with ordered mesopores connected through narrow micropores can be used as molecular sieve for the separation of linear and branched alkanes.[14] Moreover, HPCs with ordered or disordered structures had also been tested as electrodes for supercapacitors or batteries, showing that the well-connected hierarchical micro-mesopore structure provides short diffusion paths for ions and electrons, resulting in high-rate capabilities of the assembled energy storage devices.[15,16]

HPCs are normally synthesized by either hard- or soft-template methods. In the former, an inorganic material is used as a template around which the carbon precursor is polymerized, then this composite is carbonized, and the template needs to be removed in a subsequent step. In soft-template methods, a surfactant is used as a template that, along with the carbon precursor, forms a mesophase; upon carbonization, the surfactant is eliminated, creating mesopores.[17] Although carbon precursors of petrochemical origin such as resorcinol or phenolic resins have been extensively employed to produce HPCs, the use of biomass-derived precursors such as cellulose, glucose, lignin and condensed tannins, among others, has increased over the last decades in the search for "greener" technologies and processes.[18] In this sense, different research groups have successfully produced high added-value materials

from condensed tannins, particularly, HPCs by a microwave-assisted method,[19,20] using either silica hard templates [21] or soft-template methods such as evaporation-induced self-assembly (EISA),[22] phase separation [23,24] and mechano-synthesis.[25,26] The final properties of the synthesized HPCs, such as porosity, surface chemistry, stability and conductivity, depend largely on the chosen precursor/template pair. In order to understand the observed phenomena related to the use of HPCs in different applications, a thorough characterization of their physicochemical properties is of utmost importance, especially that of their porosity. For this purpose, the acquisition of gas (N_2, Ar, CO_2 or H_2) adsorption-desorption isotherms coupled with Grand Canonical Monte Carlo simulations [27–29] or the application of different density functional theory (DFT) models to these isotherms allows obtaining the pore size distribution (PSD). DFT approaches are among the most widely used tools for the textural characterization of HPCs,[1,30,31] must likely due to their commercial availability as software. However, the obtained PSD and the derived values, *e.g.*, average pore widths or surface area, depend on the assumptions of the applied model.[32]

Pore shape is an essential factor in calculating the gas adsorption models used to analyze PSDs. In the case of templated micro-mesoporous HPCs, the most common pore shapes assumed in gas adsorption modeling are slits for micropores created during carbonization and cylinders for mesopores resulting from the templating process.[33,34] The gas adsorption potential is stronger in cylindrical pores than in slits of the same width, therefore the theoretical adsorption isotherm calculated for a cylindrical pore of a given width is shifted to a lower pressure than that for a slit pore. Consequently, the PSD calculated from a given isotherm using the cylindrical model will be shifted to larger pore sizes than that of the slit pore model; hence, the results are affected by an inherent ambiguity related to the pore shape assumption. In an effort to overcome this uncertainty, this work aims to present a comprehensive approach where the desorption branch of N_2 isotherms is considered an

equilibrium branch [31] and is analyzed using a dual-shape 2D non-local DFT model for heterogeneous surface (2D-NLDFT-HS).[34] For simplicity, herein, the new dual-shape 2D-NLDFT-HS model is referred to as the DS-HS model. In this model, the slit-shape kernel is applied to pore widths $w < w_s$ and the cylinder-shape kernel to $w > w_c$, where the parameters w_s and w_c are the upper and lower bounds of the slit and cylinder kernels, respectively. These limits are not known *a priori*, but in our approach they can be adjusted interactively based on the analysis results. In this way, the model allows defining overlapping ranges of pore shapes to account for cases of mixed pore shape, i.e., $w_s > w_c$, similarly to the previously studied case of combined slit and channel finite pores across the whole range of pore sizes.[35] In this work, the dual-gas analysis method is applied,[36] in which the DS-HS model and the 2D-NLDFT-HS model for CO_2 [36] are fitted simultaneously to the N_2 and CO_2 isotherms to obtain a single PSD. Both adsorption isotherms were measured on a series of activated ordered mesoporous carbons (OMCs) reported earlier.[15] The PSD results obtained using the new approach are then compared to those calculated using the hybrid quenched solid DFT (QSDFT) model.[33,37]

2. Experimental

2.1. Raw materials

Mimosa tannin kindly provided by the company SilvaChimica (St Michele Mondovi, Italy), and commercialized as Fintan OP, was used as carbon precursor, and Pluronic® F127 (Sigma-Aldrich) was used as pore-directing agent. The materials were used as received.

2.2. Synthesis of activated micro-mesoporous OMCs

Activated micro-mesoporous OMCs were synthesized by a surfactant-water-assisted mechanochemical meso-structuration (SWAMM) method and physically activated as detailed elsewhere.[25] Briefly, tannin (T), surfactant (Pluronic: P) and water (W) were mixed in a

planetary ball mill (PM100, Retsch) in a T:P:W mass ratio of 2:0.75:1.75 g. After 60 min of milling, a mesophase was recovered and was directly subjected to carbonization at 900 °C under N_2 flow. The resulting OMC was ground to reduce the particle size and placed in an oven for activation. The temperature was raised to 900 °C under N_2 atmosphere, then the gas flow was changed to CO_2 and the temperature was held for times ranging from 15 to 105 min. Finally, the material was left to cool naturally under N_2 flow. Herein, the activated OMCs are referred to as A-*t*, where *t* stands for the activation time in minutes.

2.3. Characterization of materials

As specified in our previous study,[15] N_2 and CO_2 adsorption isotherms were acquired with ASAP 2020 and ASAP 2420 devices (Micromeritics) at 77 and 273 K, respectively. Prior to data acquisition, the samples were degassed at 110 °C under secondary vacuum for at least 48 h.

Transmission electron microscopy (TEM) images were obtained using a JEM-ARM 200F Cold FEG TEM/STEM (Jeol). For observation, powdered samples were dispersed in ethanol by low-power sonication, and then a drop of suspension was deposited on a TEM grid (carbon-coated copper, 200 mesh). From these TEM images, histograms of pore widths in the mesoporous range were obtained using the Fiji image processing software (ImageJ, version 1.52i) and its “analyze particles” tool. A detailed explanation of the methodology employed is provided in the Supporting information (SI).

3. Dual-shape 2D-NLDFT-HS (DS-HS) model

As mentioned in the introduction, the DS-HS model uses two 2D-NLDFT-HS kernels to fit the desorption branch of the experimental N_2 isotherm: the previously developed slit-shape kernel 2D-HS-SLIT (K_{slit}) [38] and the recently developed cylinder-shape kernel 2D-HS-CYL

(K_{cyl}).[34] These kernels were calculated as equilibrium ones considering the heterogeneous rough surface of the pore walls. Their theoretical isotherms do not show layering transitions, thus eliminating the artifacts associated with such transitions observed in the PSD results calculated from standard NLDFT kernels.[37,38] It is important to note that the experimental desorption data was only recorded down to a relative pressure of ~10^{-3}, so in order to have a "complete" branch, the experimental adsorption branch was used to append the desorption data to the lowest measured relative pressures. This merging of the adsorption and desorption branches is carried out considering that the process of gas adsorption is reversible in the low-pressure region, associated with micropores.

It is assumed that the effective PSD function is a sum of functions representing the slit and cylindrical pores:

$$PSD = PSD_{slit} + PSD_{cyl} \quad (1)$$

so the total N_2 isotherm (Q_{N2}) is given by the sum of the following integrals:

$$Q_{N2}(x) = \int_{0.36\ nm}^{w_s} PSD_{slit}(w)K_{slit}(w,x)dw + \int_{w_c}^{50\ nm} PSD_{cyl}(w)K_{cyl}(w,x)dw \quad (2)$$

where x is the relative pressure and the lower limit of 0.36 nm for the first term corresponds to the minimum detectable pore size determined and which is related to the kinetic diameter of the N_2 molecule.

In the initial version of the DS-HS model,[34] both shape limits w_s and w_c were equal to 2 nm; in the present version, these limits are adjustable and are set based on the analysis results.

Additionally, the CO_2 isotherm at 273 K might be fitted simultaneously with the N_2 isotherm, using the 2D-HS kernel for CO_2 (K_{CO2}).[36] Because CO_2 adsorption at 273 K below 1 atm is highly sensitive to the size of ultramicropores (w < 0.7 nm) and it has very low sensitivity in the mesopore range,[36,39] this isotherm is fitted only in the range of slit pores where the following integral gives the theoretical adsorption isotherm:

$$Q_{CO2}(x) = \int_{0.36\,nm}^{w_s} PSD_{slit}(w) K_{CO2}(w, x) dw \quad (3)$$

4. Results and discussion

The adsorption data recently reported on a series of CO_2-activated OMCs [15] provides an excellent opportunity to analyze and describe the progression of pore structure changes upon activation of these HPCs in a detailed and systematic manner. The database of adsorption isotherms for the studied series of activated carbons consists of eight N_2 isotherms measured at 77 K and eight CO_2 isotherms measured at 273 K. The samples are denoted by A-*t*, where *t* represents the activation time in minutes, the initial non-activated carbon sample being referred to as OMC. The results of applying the DS-HS model to the isotherm database and the effect of varying the limits w_s and w_c are discussed below.

4.1. PSD analysis assuming a slit-cylinder boundary at $w_s = w_c = 2$ nm

In the first step of data analysis, the theoretical isotherms given by Equations (2) and (3) were simultaneously fitted to the corresponding experimental N_2 and CO_2 isotherms. As mentioned above, the desorption branch of the N_2 isotherm is considered an equilibrium branch. The fitting is performed using the SAIEUS program, as detailed in earlier works.[34,36,40] In this first step of data analysis, it is assumed, as it was done before, that the slit and cylinder model limits are equal to 2 nm: $w_s = w_c = 2$ nm. Selected fitting results for the least activated, moderately activated, and most activated samples (A-15, A-60, and A105) are shown in Figure 1, and the results for the remaining samples are shown in Figure S1. The calculated isotherms accurately fit the experimental points for all samples and the PSDs resulting from the fits are shown for all samples in Figure 2. The fact that textural properties of the carbon samples change systematically upon gradual activation allows for a logical

interpretation of their PSD evolution. Clearly, the micropore peak broadens to larger pores with increasing activation time. In contrast, the mesopore peak resulting from the templating process remains symmetric in the same position, showing an increase in the volume of these pores. These textural changes can be explained by the burn-off of the carbon material on the pore walls, which causes the micropores to widen and the mesopore surface to become coarser. The increase in coarseness and irregularity of the mesopore surface is reflected by the widening of the mesopore peak in the calculated PSD associated with the less steep transition step on the desorption isotherms, as seen for example in Figure1.

Tabular data describing the textural parameters obtained from the PSDs calculated with the slit-cylinder boundary at $w_s = w_c = 2$ nm are included in Table 1 and discussed in Section 4.2.

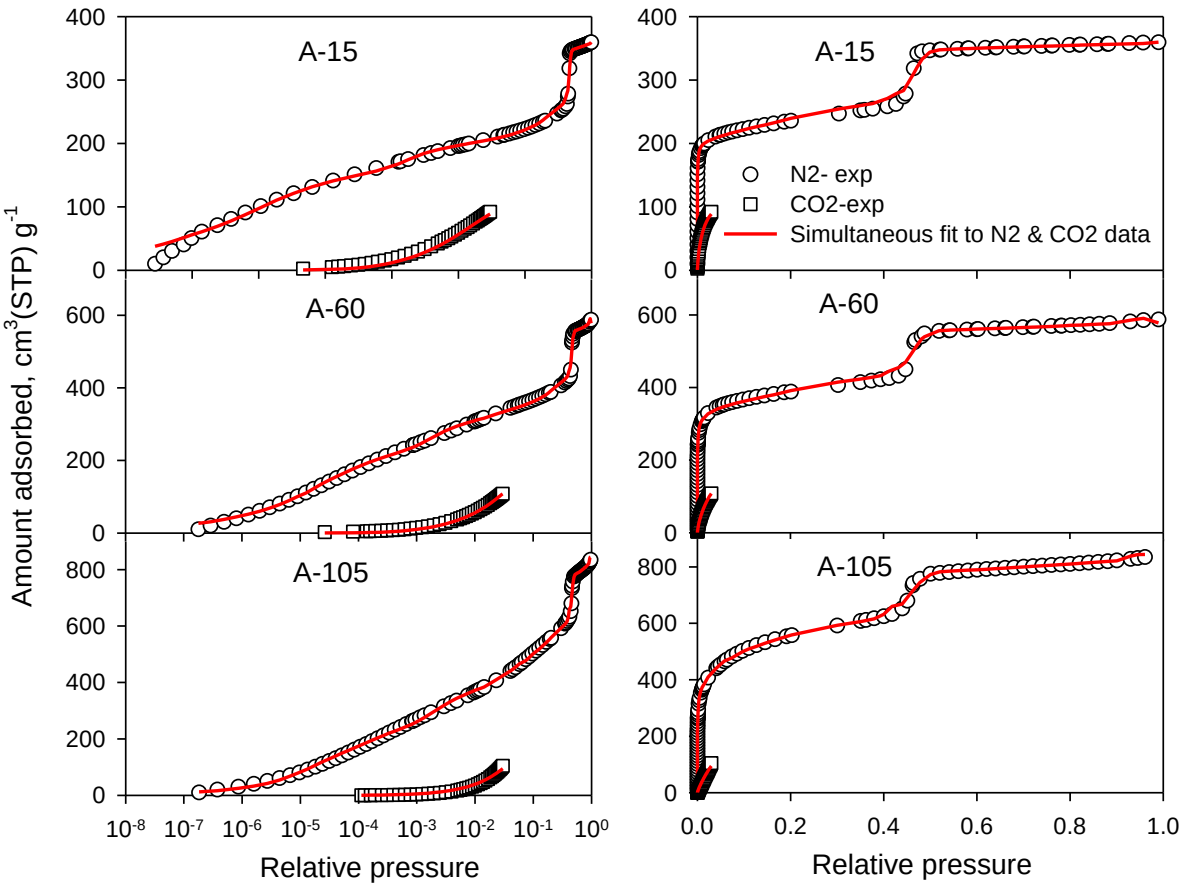

Figure 1. Selected experimental branches of N_2 desorption and CO_2 adsorption isotherms (circular and square symbols, respectively) for A-15, A-60, and A-105 samples, in logarithm and linear scales (left and right column, respectively). The lines show the results from the simultaneous fits of the DS-HS kernel and the 2D-HS kernel for CO_2 to the corresponding N_2 and CO_2 isotherms, assuming a slit-cylinder boundary at $w_s = w_c = 2$ nm.

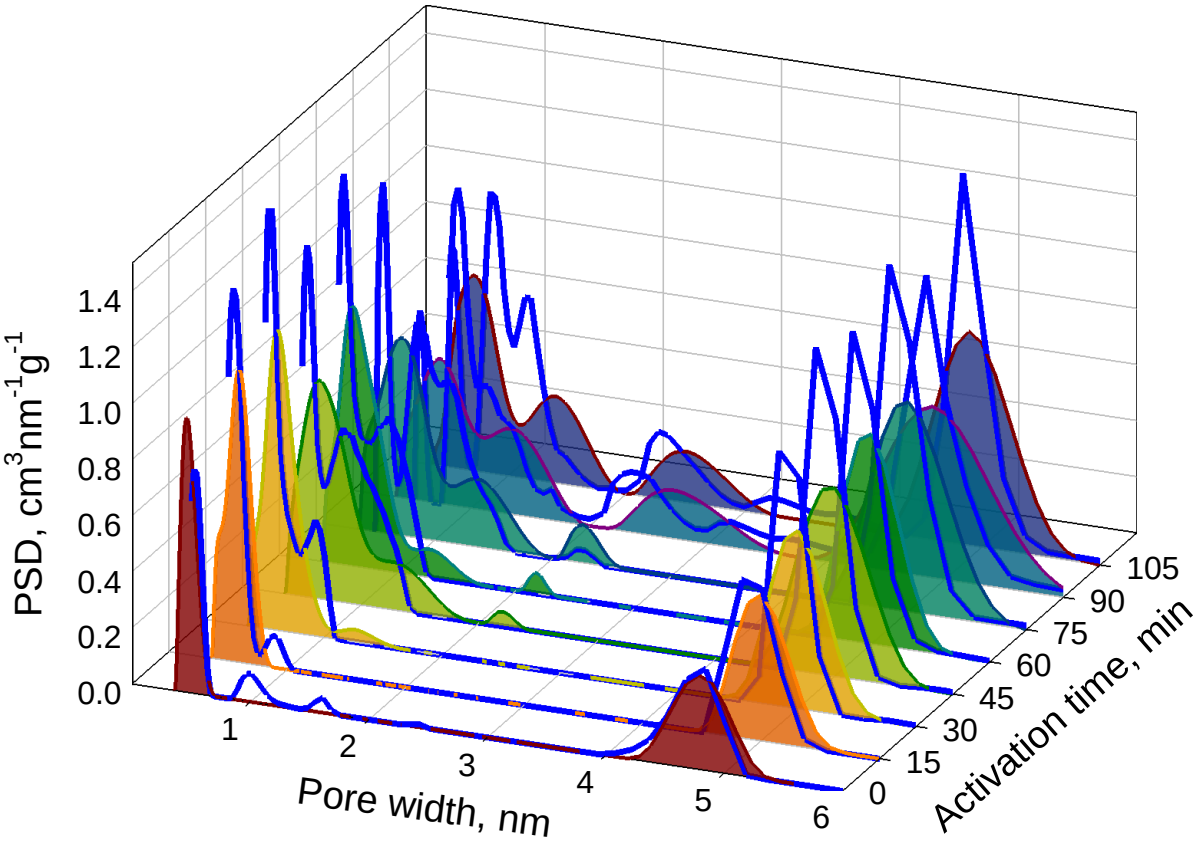

Figure 2. PSDs calculated using the DS-HS model assuming a slit pores in the width range 0.36 – 2 nm and cylindrical pore shapes for $w > 2$ nm shown as color-filled plots. The results were obtained by simultaneously fitting the model to the corresponding N_2 desorption and CO_2 adsorption isotherm branches. The solid blue lines show the results of the hybrid QSDFT model.

It is interesting to compare the PSD calculations of the DS-HS model with the results obtained using the Versa-win (version 2.0) software, which is often used to analyze the textural properties of porous carbons. Several kernels are available in this software, including

the carbon kernels described earlier by Gor et al.[33] For the analysis of the A-*t* series, the hybrid QSDFT kernel was applied here, consisting of equilibrium isotherms calculated for both slit and cylindrical pore models, where the range of slit-cylinder boundary is fixed at 2 nm, *i.e.*, $w_s = w_c = 2$ nm. This kernel is applied for the analysis of the desorption branch of the N_2 isotherm like our model. The results from the hybrid QSDFT model are presented in Figure 2 (solid blue lines) along with those obtained from the DS-HS model.

Even though the two methods are based on different assumptions and the QSDFT is a one-dimensional model, the results show qualitatively reasonable agreement between the PSDs calculated by these methods. A more detailed view of the results shows that the DS-HS model gives smooth and continuous PSDs while the PSD plots calculated using the hybrid QSDFT model show sharp peaks and discontinuities. Furthermore, the DS-HS distributions calculated by the SAIEUS program [34,36,40] originate and terminate at zero on the y-axis. In contrast, the hybrid QSDFT distributions originate at relatively high values on that axis. Because the multiple plots in Figure 2 may be difficult to examine, Figure 3 shows the PSD results for a single sample, A-105, which more clearly illustrates the mentioned differences.

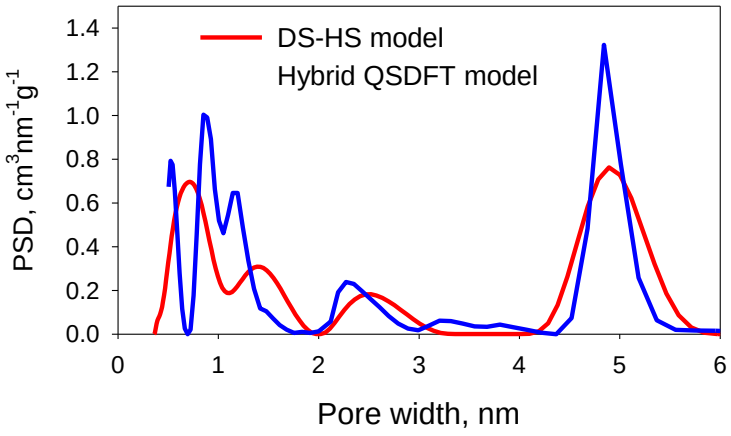

Figure 3. Comparison of PSD results calculated using two methods: the dual-shape DS-HS pore model and the hybrid QSDFT model.

4.2. PSD analysis assuming a slit-cylinder boundary at $w_s = w_c = 3$ nm

It is logical to expect a systematic trend of PSD variations with increasing activation time. Such a trend is indeed observed for non-activated and slightly activated samples. However, this trend is broken for samples activated for $t \geq 45$ min, where unexpected peaks begin to appear for $w > 2$ nm. We suspect that this is an artifact due to the change of applied model at 2 nm from slit to cylinder. To test this hypothesis, the isotherms of the sample activated for the longest time (105 min) were analyzed using two additional pore shape limits, (i) $w_s = 3$ nm and $w_c = 2$ nm, and (ii) $w_s = w_c = 3$ nm. Comparison of the calculation results shows significant differences in the PSDs depending on the assumed shape limits (Figure 4a) and practically no difference in the fitted isotherms as shown in Figure 4b. The accepted shape limits cannot be verified based on the goodness of the model fit, but the fact that the additional peak appears above 2 nm when $w_c = 2$ nm indicates the interference of the cylindrical model in this transition part of the PSD. Recalling that the origin of the slit micropores is the carbonization process followed by the activation which widens these pores, there is no reason to assume the presence of cylindrical pores near $w = 2$ nm. Based on these observations, we consider that, for the samples under study, the boundary between the slit and cylindrical pore models should be $w_s = w_c = 3$ nm. This logical conclusion, obtained from the elegant systematic trend in the PSD variation for our samples, is however not universal. Other carbon materials may have different properties, which may be investigated using this interactive approach.

Nevertheless, in the second step of our data analysis, the slit-cylinder boundary is assumed to be 3 nm.

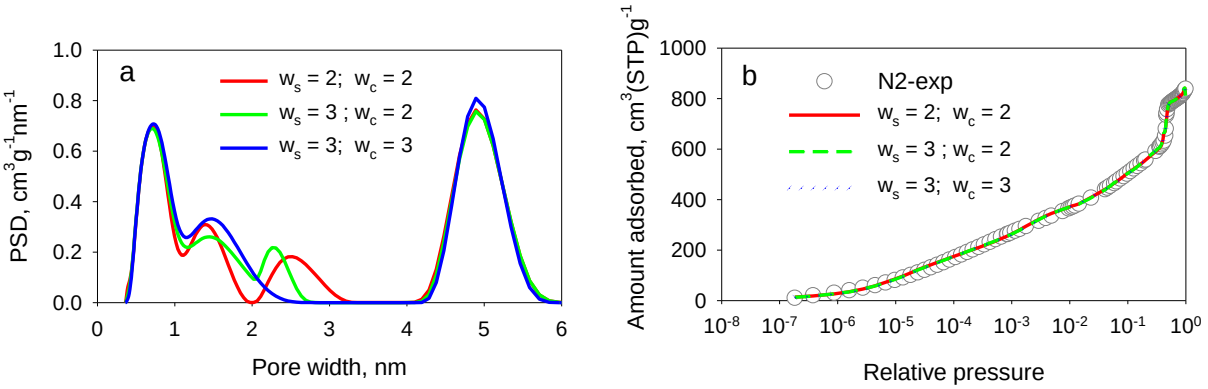

Figure 4. PSD analysis of isotherms of the OMC sample activated for 105 min (A-105). (a) Calculated PSDs, (b) fitted isotherm curves. The DS-HS model was applied to fit the experimental data (circular symbols) using different shape limits, w_s and w_c, as indicated in the legends.

Figure 5 presents the PSDs calculated in this way (with $w_s = w_c = 3$ nm), now exhibiting a regular trend in their variations with increasing activation time. Again, there is practically no difference between fitting curves (not shown) of the different shape models for all samples. The high accuracy observed in the simultaneous fit of N_2 and CO_2 isotherms (Figure 1 and Figure S1) for all activated OMC samples indicates that the N_2 isotherms are well equilibrated. In contrast, it was previously reported that deviations of the dual-gas fit of N_2 and CO_2 isotherms indicated an under-equilibrated state of the N_2 isotherm at low relative pressure due to slow diffusion into the carbon ultra-micropores.[41] Such a deviation is observed for the non-activated OMC sample in Figure 6a, again indicating a minor under-equilibration of the N_2 isotherm at low relative pressures. Despite the perfect fit of the N_2 kernel to the individual N_2 isotherm shown in this figure, because of the equilibration problem at low relative pressure, we consider that the CO_2 isotherm provides better information about the ultra-micropores in the OMC sample. To provide the most accurate PSD characterization of this sample, the full CO_2 isotherm was simultaneously fitted with the higher-pressure part

of the N_2 isotherm, see Figure 6b. Figure 6c compares the PSDs obtained from the fitting of (i) full N_2 and CO_2, (ii) full N_2 and (iii) full CO_2 and high-pressure N_2 isotherms. From this comparison, it can be observed that the micropore peak obtained from analysis (iii) is shifted to a value about 0.1 nm lower than that calculated using the N_2 isotherm alone (ii). This shift can be seen in Figure 5 where the PSDs calculated from the single N_2 isotherm (dotted line plots) show good agreement with those calculated from both N_2 and CO_2 isotherms for all samples except the non-activated one. The analysis of this series of carbon materials shows the advantage of using the dual-gas model that allows for the detection of under-equilibrated N_2 isotherms, which in turn allows for better understanding of the data and improved PSD results.

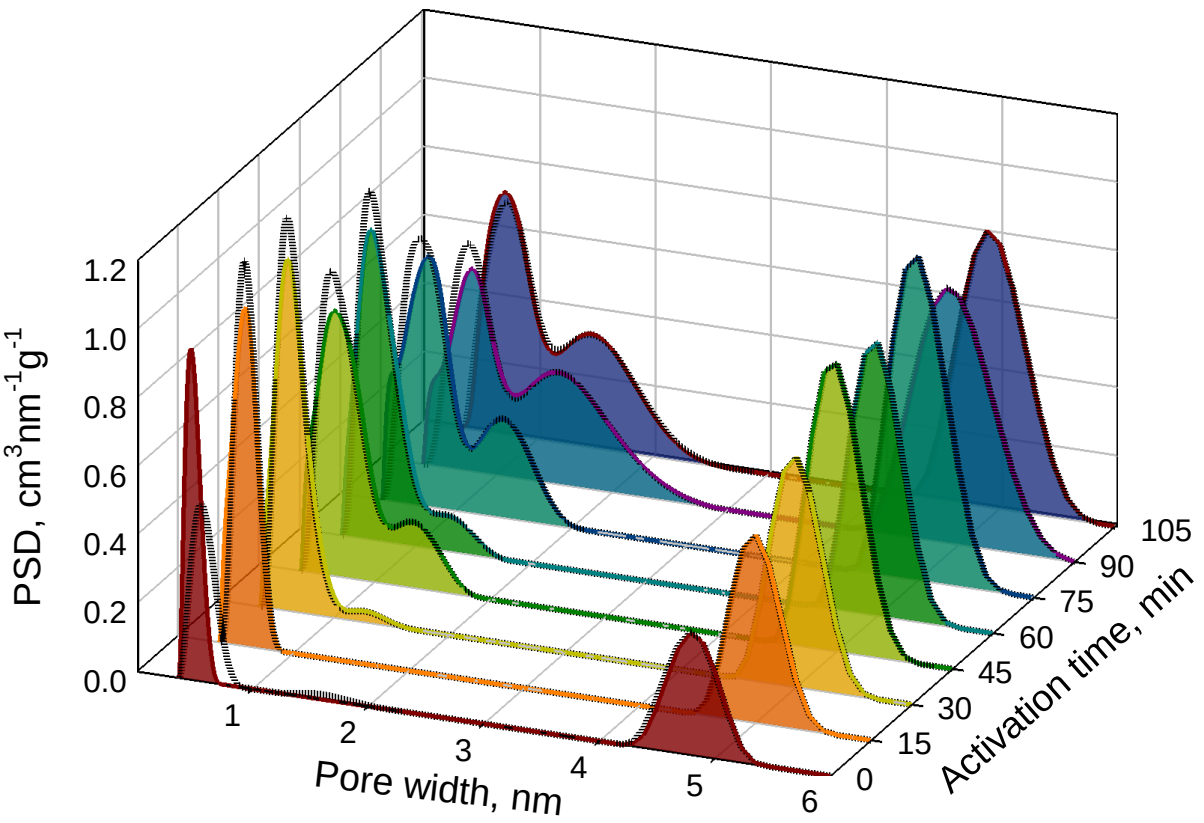

Figure 5. PSDs calculated using the DS-HS model assuming a slit-cylinder boundary at w_s = w_c = 3 nm. The color-filled plots were obtained by simultaneously fitting the model to the

corresponding N_2 desorption and CO_2 adsorption isotherm branches. The dotted black lines represent the results obtained only from the N_2 desorption isotherms.

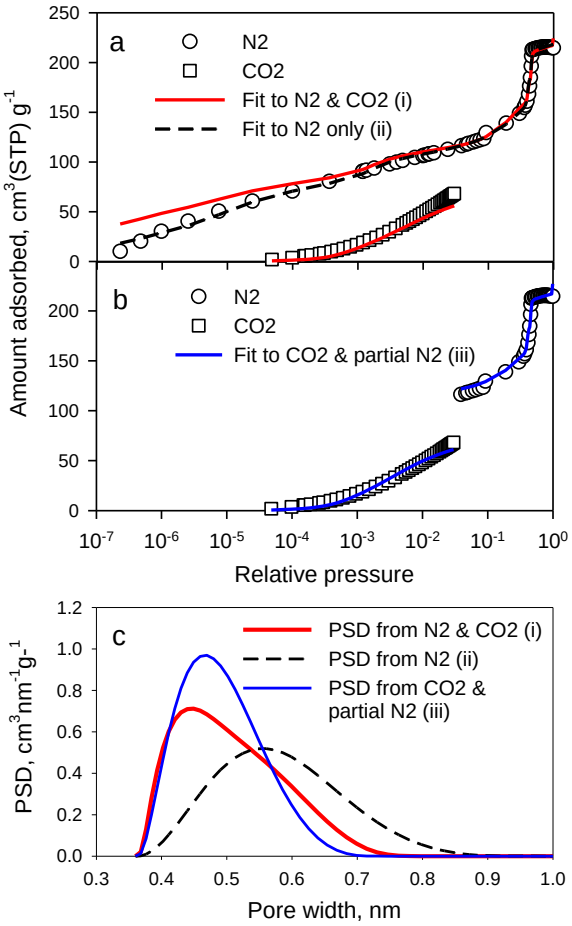

Figure 6. PSD analysis of the non-activated OMC sample. (a) Fit of the full N_2 and CO_2 isotherms. (b) Fit of the higher-pressure part of N_2 and full CO_2 isotherms. (c) PSDs calculated from different combinations of adsorption isotherms.

In an attempt to validate the mesopore characteristics obtained from the DS-HS model (w_s = w_c = 3 nm), the mesoporous parts of the PSDs are shown in Figure 7 alongside TEM images and their associated pore width histograms obtained by image of OMC, A75, and A90 samples processing (see details in Figure S2 and related text in the SI). In the mesopore range,

the peak of the PSDs remains almost unchanged and widens after activation from ~1 to ~ 2 nm, measured at the base of the peak (Figure 7d-f). The histograms from TEM image processing are significantly broader and do not follow the same trend (Figure 7a-c). Image processing indeed highly depends on the quality of the image and on the processing procedure (contrast, definition, processing algorithm, among others). For example, the criterion for choosing the value of the threshold parameter can be very subjective and can change the results considerably; in particular, Figure S3 shows that varying the threshold from 10 to 20 % can change the peak center of the histograms from 4.3 to 5.1 nm. Thus, in these cases, the results of textural characterization of the mesopores from image processing of OMC, A-75 and A-90 must be considered with caution. In addition, the image processing focuses only on a specific particle (the one captured in the image) whereas the PSDs obtained from the adsorption isotherm analysis provide an average of the information obtained from many particles. Nonetheless, Figure 7 shows that the PSDs are within the range of the corresponding histograms, which demonstrates an approximate qualitative agreement between the two descriptions.

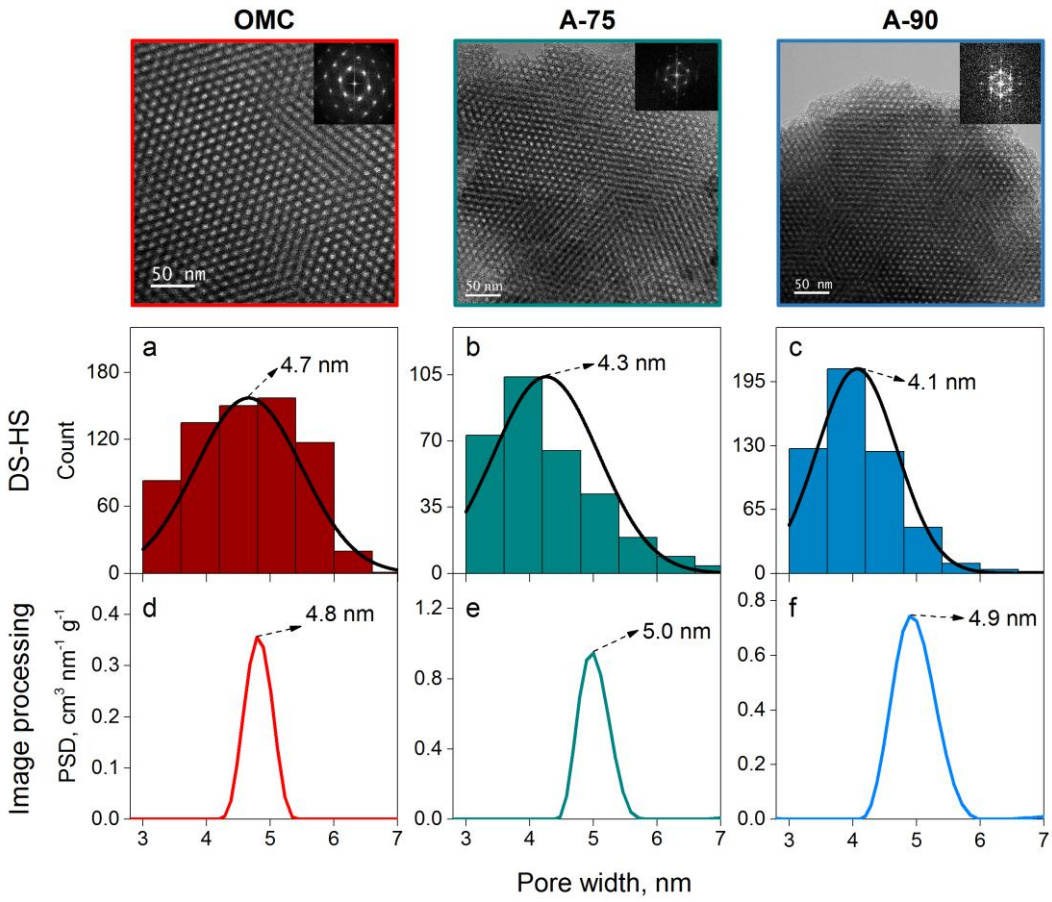

Figure 7. TEM images of OMC, A-75, and A-90 samples (top). (a-c) Histograms of pore widths obtained from TEM image processing and (d-f) PSDs calculated using the DS-HS model assuming slit-cylinder boundary at $w_s = w_c = 3$ nm.

For a complete pore characterization of activated OMCs, Table 1 presents textural parameters commonly reported for porous carbon materials and the volume and surface area of slit pores (V_{slit} and S_{slit}, respectively) calculated with the new DS-HS model with slit-cylinder boundary at $w_s = w_c = 3$ nm. Primary values in Table 1 were calculated for the model with slit-cylinder boundary at $w_s = w_c = 3$ nm; the values in brackets represent the differences between the quantities calculated with the shape boundaries at 3 and 2 nm. It is important to note that, as expected, the most significant differences between textural parameters calculated for the two boundaries appear for samples with a higher degree of activation for $t \geq 45$ min, where the artifacts occurred on the PSDs calculated using the model with the 2 nm shape

boundary. For both boundary values the increments in total surface areas are relatively smaller than those in total pore volumes; this difference is to be expected because the pore volume increases with the pore width, while surface area decreases with the pore width.

Table 1. Textural parameters calculated using the DS-HS model. Primary values were calculated for the model with $w_s = w_c = 3$ nm, values in brackets represent the differences between the quantities calculated with the shape boundaries at 3 and 2 nm.

Sample	S_{total} ($m^2\ g^{-1}$)	V_{total} ($cm^3\ g^{-1}$)	V_{meso} ($cm^3\ g^{-1}$)	V_{μ} ($cm^3\ g^{-1}$)	S_{slit} ($m^2\ g^{-1}$)	V_{slit} ($cm^3\ g^{-1}$)	$Peak_{meso}$ (nm)
OMC	797 (43)	0.35	0.20	0.15	639 (49)	0.16 (0.01)	4.8
A-15	1151 (-5)	0.55	0.29	0.26	920 (-6)	0.26	5.0
A-30	1407 (-3)	0.73	0.38	0.35	1112 (-3)	0.35	5.0
A-45	163 (-4)	0.97	0.51 (-0.01)	0.46 (0.01)	1246 (17)	0.4 (0.01)	5.0
A-60	1568 (-8)	0.89	0.47 (-0.01)	0.42 (0.01)	1212 (13)	0.42 (.01)	5.0
A-75	1729 (-15)	1.16	0.64 (-0.04)	0.52 (0.04)	1260 (56)	0.52 (0.04)	5.0
A-90	1697 (-49)	1.30 (-0.01)	0.76 (-0.11)	0.54 (0.011)	1180 (181)	0.59 (0.16)	4.9
A-105	1755 (-45)	1.25	0.67 (-0.11)	0.58 (0.10)	1272 (154)	0.60 (0.12)	4.9

S_{total} and V_{total} : total surface and volume; V_{meso} volume of pores between 2 and 50 nm; V_{μ} volume of pores under 2 nm; S_{slit} and V_{slit} surface and volume of pores with slit geometry; $Peak_{meso}$ pore diameter where the peak of the mesopore size distribution is located.

The DS-HS model is again compared to the hybrid QSDFT model in Figure 8 where overall agreement is observed between the two models for the calculated average pore volume, surface area and pore volume in the range of pore widths up to 6 nm ($w_{av,<6nm}$, $S_{<6nm}$ and $V_{<6nm}$, respectively). However, it should be noted that $w_{av,<6nm}$ determined by the hybrid QSDFT model is larger than that determined by the DS-HS model for OMC, A-15 and A-30, where the fraction of ultra-micropores is higher (Figure 8a). This is because the hybrid QSDFT only fits N_2 isotherms, while our method also fits CO_2 adsorption data. CO_2

molecules have easier access to the narrower micropores, thus allowing a better assessment of the ultra-microporosity, as previously mentioned. The differences in $w_{av,<6nm}$ determined by both models become smaller with activation, which reduces the percentage of ultra-microporosity and thus the number of pores only accessible to CO_2 molecules. Additionally, Figures 8d and 8e compare the contributions to pore volume and surface area in the 2 – 4 nm range for samples A-75, A-90, and A-105, from which it is clear that the hybrid QSDFT model has a larger contribution related to artifact peaks resulting from the transition at the assumed slit-cylindrical shape boundary. It is worth realizing here that the small contributions to pore volume and surface area calculated from the DS-HS model in this range for samples A-90 and A-105 are due to the widening of the microporosity, which is not considered an artifact (see Figure 5).

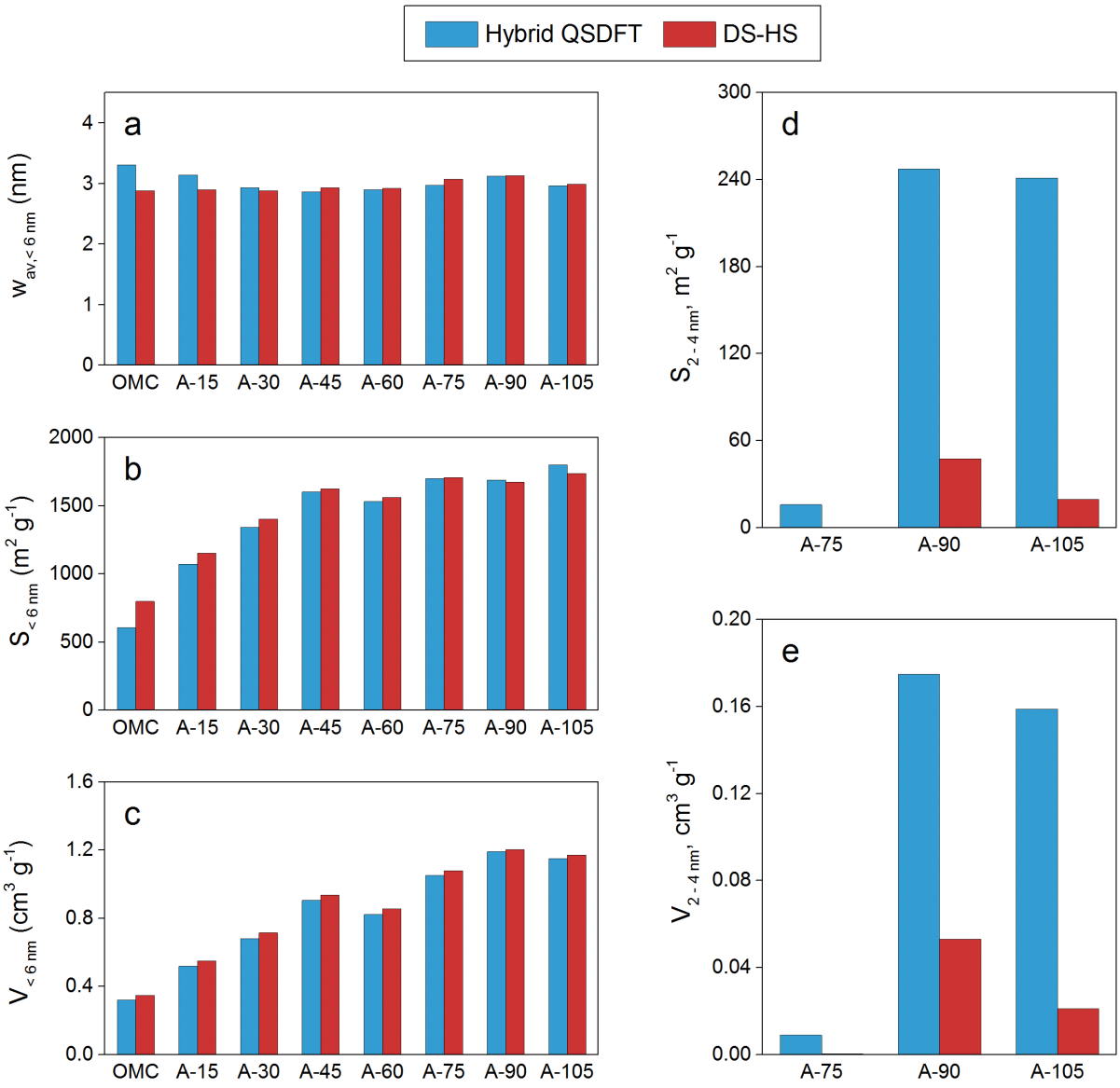

Figure 8. Textural properties calculated with DS-HS and hybrid QSDFT models: (a) average pore volume ($w_{av,<6\ nm}$), (b) surface area ($S_{<6\ nm}$) and pore volume ($V_{<6\ nm}$) in the full range of pore widths up to 6 nm; contributions to (d) surface area and (e) pore volume in the range of width from 2 to 4 nm ($S_{2–4\ nm}$ and $V_{2–4\ nm}$, respectively).

5. Conclusion

In the present study, a new version of the dual-shape 2D-NLDFT-HS (DS-HS) model is used for the textural characterization of hierarchical porous carbons. The DS-HS model uses the 2D-NLDFT-HS kernels developed for slit and cylindrical pore shapes to fit the

experimental N_2 adsorption data and introduces the possibility of adjusting the slit-cylindrical pore shape ranges. Based on the analysis of our series of hierarchical porous carbons with increasing degree of activation, it was found that the slit-cylinder boundary traditionally set at 2 nm appeared to cause artifacts on the PSD calculated for highly activated carbons. A logical conclusion was reached thanks to the elegant systematic trend of the PSD variation for our samples. The appropriate shape boundary for our samples should be 3 nm, eliminating these artifacts. This result is not universal, however, and other carbon materials may have different properties, which may be investigated using this interactive approach.

In addition, the dual-gas analysis method allows for the simultaneous fitting of N_2 and CO_2 kernels to the corresponding isotherm data, which has led to a more accurate description of the PSDs in the ultra-micropore range. Since the slit-cylinder boundary is not independently proven and is often arbitrarily set at 2nm, the ability to adjust and investigate its effects in the DS-HS model is a significant advantage over methods using a fixed boundary, as exemplified by the comparison with the hybrid QSDFT model performed as part of this study.

Supporting information

Document containing additional figures and an explanation of the methodology followed for processing TEM images.

Acknowledgment

J.J. would like to thank Dr. Jeffrey Kenvin of Micromeritics for creative discussions on the data deconvolution methods used in this work. J.C.G. gratefully acknowledges CONACYT-SENER (601021/438978) for the assigned scholarship to support her PhD studies, resulting in the work presented here. This study was partly supported by the French PIA project “Lorraine

Université d'Excellence", reference ANR-15-IDEX-04-LUE, and the TALiSMAN project, funded by ERDF (2019-000214).

References

(1) Thommes, M.; Kaneko, K.; Neimark, A. V.; Olivier, J. P.; Rodriguez-Reinoso, F.; Rouquerol, J.; Sing, K. S. W. Physisorption of Gases, with Special Reference to the Evaluation of Surface Area and Pore Size Distribution (IUPAC Technical Report). *Pure Appl. Chem.* **2015**, *87* (9–10). https://doi.org/10.1515/pac-2014-1117.

(2) Singh, G.; Lakhi, K. S.; Sil, S.; Bhosale, S. V.; Kim, I.; Albahily, K.; Vinu, A. Biomass Derived Porous Carbon for CO2 Capture. *Carbon* **2019**, *148*, 164–186. https://doi.org/10.1016/j.carbon.2019.03.050.

(3) Saufi, S. M.; Ismail, A. F. Fabrication of Carbon Membranes for Gas Separation—a Review. *Carbon* **2004**, *42* (2), 241–259. https://doi.org/10.1016/j.carbon.2003.10.022.

(4) ben Mosbah, M.; Mechi, L.; Khiari, R.; Moussaoui, Y. Current State of Porous Carbon for Wastewater Treatment. *Processes* **2020**, *8* (12), 1651. https://doi.org/10.3390/pr8121651.

(5) Zhang, Y.; Yang, L.; Yan, L.; Wang, G.; Liu, A. Recent Advances in the Synthesis of Spherical and NanoMOF-Derived Multifunctional Porous Carbon for Nanomedicine Applications. *Coord. Chem. Rev.* **2019**, *391*, 69–89. https://doi.org/10.1016/j.ccr.2019.04.006.

(6) De, S.; Balu, A. M.; van der Waal, J. C.; Luque, R. Biomass-Derived Porous Carbon Materials: Synthesis and Catalytic Applications. *ChemCatChem* **2015**, *7* (11), 1608–1629. https://doi.org/10.1002/cctc.201500081.

(7) Quílez-Bermejo, J.; Morallón, E.; Cazorla-Amorós, D. Metal-Free Heteroatom-Doped Carbon-Based Catalysts for ORR: A Critical Assessment about the Role of Heteroatoms. *Carbon* **2020**, *165*, 434–454. https://doi.org/10.1016/j.carbon.2020.04.068.

(8) Roberts, A. D.; Li, X.; Zhang, H. Porous Carbon Spheres and Monoliths: Morphology Control, Pore Size Tuning and Their Applications as Li-Ion Battery Anode Materials. *Chem. Soc. Rev.* **2014**, *43* (13), 4341–4356. https://doi.org/10.1039/C4CS00071D.

(9) Castro-Gutiérrez, J.; Fierro, V.; Celzard, A. Energy Storage in Supercapacitors: Focus on Tannin-Derived Carbon Electrodes. *Front. Mater.* **2020**, *7*, 217. https://doi.org/10.3389/fmats.2020.00217.

(10) Pérez-Rodríguez, S.; Alegre, C.; Sebastián, D.; Lázaro, M. J. Chapter 10 - Emerging Carbon Nanostructures in Electrochemical Processes. In *Emerging Carbon Materials for Catalysis*; Sadjadi, S., Ed.; Elsevier, 2021; pp 353–388. https://doi.org/10.1016/B978-0-12-817561-3.00010-X.

(11) Yang, S. J.; Jung, H.; Kim, T.; Park, C. R. Recent Advances in Hydrogen Storage Technologies Based on Nanoporous Carbon Materials. *Prog. Nat. Sci. Mater. Int.* **2012**, *22* (6), 631–638. https://doi.org/10.1016/j.pnsc.2012.11.006.

(12) Benzigar, M. R.; Talapaneni, S. N.; Joseph, S.; Ramadass, K.; Singh, G.; Scaranto, J.; Ravon, U.; Al-Bahily, K.; Vinu, A. Recent Advances in Functionalized Micro and Mesoporous Carbon Materials: Synthesis and Applications. *Chem. Soc. Rev.* **2018**, *47* (8), 2680–2721. https://doi.org/10.1039/C7CS00787F.

(13) *Green Carbon Materials: Advances and Applications*; Rufford, T. E., Hulicova-Jurcakova, D., Zhu, J., Eds.; Pan Stanford Publishing: Singapore, 2014.
(14) Castro-Gutiérrez, J.; De Oliveira Jardim, E.; Canevesi, R. L. S.; Silvestre-Albero, J.; Kriesten, M.; Thommes, M.; Celzard, A.; Fierro, V. Molecular Sieving of Linear and Branched C6 Alkanes by Tannin-Derived Carbons. *Carbon* **2021**, *174*, 413–422. https://doi.org/10.1016/j.carbon.2020.12.061.
(15) Castro-Gutiérrez, J.; Díez, N.; Sevilla, M.; Izquierdo, M. T.; Ghanbaja, J.; Celzard, A.; Fierro, V. High-Rate Capability of Supercapacitors Based on Tannin-Derived Ordered Mesoporous Carbons. *ACS Sustain. Chem. Eng.* **2019**, *7* (21), 17627–17635. https://doi.org/10.1021/acssuschemeng.9b03407.
(16) Díez, N.; Ferrero, G. A.; Sevilla, M.; Fuertes, A. B. A Simple and General Approach for *in Situ* Synthesis of Sulfur–Porous Carbon Composites for Lithium–Sulfur Batteries. *Sustain. Energy Fuels* **2019**, *3* (12), 3498–3509. https://doi.org/10.1039/C9SE00722A.
(17) Inagaki, M.; Toyoda, M.; Soneda, Y.; Tsujimura, S.; Morishita, T. Templated Mesoporous Carbons: Synthesis and Applications. *Carbon* **2016**, *107*, 448–473. https://doi.org/10.1016/j.carbon.2016.06.003.
(18) *Porous Carbon Materials from Sustainable Precursors*; White, R. J., Ed.; Green Chemistry Series; Royal Society of Chemistry: Cambridge, 2015. https://doi.org/10.1039/9781782622277.
(19) Ramasahayam, S. K.; Nasini, U. B.; Shaikh, A. U.; Viswanathan, T. Novel Tannin-Based Si, P Co-Doped Carbon for Supercapacitor Applications. *J. Power Sources* **2015**, *275*, 835–844. https://doi.org/10.1016/j.jpowsour.2014.11.020.
(20) Bairi, V. G.; Nasini, U. B.; Kumar Ramasahayam, S.; Bourdo, S. E.; Viswanathan, T. Electrocatalytic and Supercapacitor Performance of Phosphorous and Nitrogen Co-Doped Porous Carbons Synthesized from Aminated Tannins. *Electrochimica Acta* **2015**, *182*, 987–994. https://doi.org/10.1016/j.electacta.2015.10.011.
(21) Sanchez-Sanchez, A.; Izquierdo, M. T.; Ghanbaja, J.; Medjahdi, G.; Mathieu, S.; Celzard, A.; Fierro, V. Excellent Electrochemical Performances of Nanocast Ordered Mesoporous Carbons Based on Tannin-Related Polyphenols as Supercapacitor Electrodes. *J. Power Sources* **2017**, *344*, 15–24. https://doi.org/10.1016/j.jpowsour.2017.01.099.
(22) Schlienger, S.; Graff, A.-L.; Celzard, A.; Parmentier, J. Direct Synthesis of Ordered Mesoporous Polymer and Carbon Materials by a Biosourced Precursor. *Green Chem.* **2012**, *14* (2), 313–316. https://doi.org/10.1039/C2GC16160E.
(23) Braghiroli, F. L.; Fierro, V.; Parmentier, J.; Pasc, A.; Celzard, A. Easy and Eco-Friendly Synthesis of Ordered Mesoporous Carbons by Self-Assembly of Tannin with a Block Copolymer. *Green Chem.* **2016**, *18* (11), 3265–3271. https://doi.org/10.1039/C5GC02788H.
(24) Sanchez-Sanchez, A.; Izquierdo, M. T.; Medjahdi, G.; Ghanbaja, J.; Celzard, A.; Fierro, V. Ordered Mesoporous Carbons Obtained by Soft-Templating of Tannin in Mild Conditions. *Microporous Mesoporous Mater.* **2018**, *270*, 127–139. https://doi.org/10.1016/j.micromeso.2018.05.017.
(25) Castro-Gutiérrez, J.; Sanchez-Sanchez, A.; Ghanbaja, J.; Díez, N.; Sevilla, M.; Celzard, A.; Fierro, V. Synthesis of Perfectly Ordered Mesoporous Carbons by Water-Assisted Mechanochemical Self-Assembly of Tannin. *Green Chem.* **2018**, *20* (22), 5123–5132. https://doi.org/10.1039/c8gc02295j.
(26) Zhang, P.; Wang, L.; Yang, S.; Schott, J. A.; Liu, X.; Mahurin, S. M.; Huang, C.; Zhang, Y.; Fulvio, P. F.; Chisholm, M. F.; Dai, S. Solid-State Synthesis of Ordered

Mesoporous Carbon Catalysts via a Mechanochemical Assembly through Coordination Cross-Linking. *Nat. Commun.* **2017**, *8*, 15020. https://doi.org/10.1038/ncomms15020.
(27) Barrera, D.; Dávila, M.; Cornette, V.; de Oliveira, J. C. A.; López, R. H.; Sapag, K. Pore Size Distribution of Ordered Nanostructured Carbon CMK-3 by Means of Experimental Techniques and Monte Carlo Simulations. *Microporous Mesoporous Mater.* **2013**, *180*, 71–78. https://doi.org/10.1016/j.micromeso.2013.06.028.
(28) Soares Maia, D. A.; Sapag, K.; Toso, J. P.; López, R. H.; Azevedo, D. C. S.; Cavalcante, C. L.; Zgrablich, G. Characterization of Activated Carbons from Peach Stones through the Mixed Geometry Model. *Microporous Mesoporous Mater.* **2010**, *134* (1–3), 181–188. https://doi.org/10.1016/j.micromeso.2010.05.024.
(29) Cimino, R.; Cychosz, K. A.; Thommes, M.; Neimark, A. V. Experimental and Theoretical Studies of Scanning Adsorption–Desorption Isotherms. *Colloids Surf. Physicochem. Eng. Asp.* **2013**, *437*, 76–89. https://doi.org/10.1016/j.colsurfa.2013.03.025.
(30) Jagiello, J.; Thommes, M. Comparison of DFT Characterization Methods Based on N2, Ar, CO2, and H2 Adsorption Applied to Carbons with Various Pore Size Distributions. *Carbon* **2004**, *42* (7), 1227–1232. https://doi.org/10.1016/j.carbon.2004.01.022.
(31) Landers, J.; Gor, G. Yu.; Neimark, A. V. Density Functional Theory Methods for Characterization of Porous Materials. *Colloids Surf. Physicochem. Eng. Asp.* **2013**, *437*, 3–32. https://doi.org/10.1016/j.colsurfa.2013.01.007.
(32) Ania, C. O.; Armstrong, P. A.; Bandosz, T. J.; Beguin, F.; Carvalho, A. P.; Celzard, A.; Frackowiak, E.; Gilarranz, M. A.; László, K.; Matos, J.; Pereira, M. F. R. Engaging Nanoporous Carbons in "beyond Adsorption" Applications: Characterization, Challenges and Performance. *Carbon* **2020**, *164*, 69–84. https://doi.org/10.1016/j.carbon.2020.03.056.
(33) Gor, G. Yu.; Thommes, M.; Cychosz, K. A.; Neimark, A. V. Quenched Solid Density Functional Theory Method for Characterization of Mesoporous Carbons by Nitrogen Adsorption. *Carbon* **2012**, *50* (4), 1583–1590. https://doi.org/10.1016/j.carbon.2011.11.037.
(34) Jagiello, J.; Chojnacka, A.; Pourhosseini, S. E. M.; Wang, Z.; Beguin, F. A Dual Shape Pore Model to Analyze the Gas Adsorption Data of Hierarchical Micro-Mesoporous Carbons. *Carbon* **2021**, *178*, 113–124. https://doi.org/10.1016/j.carbon.2021.02.098.
(35) Jagiello, J.; Kenvin, J.; Olivier, J. P.; Lupini, A. R.; Contescu, C. I. Using a New Finite Slit Pore Model for NLDFT Analysis of Carbon Pore Structure. *Adsorpt. Sci. Technol.* **2011**, *29* (8), 769–780. https://doi.org/10.1260/0263-6174.29.8.769.
(36) Jagiello, J.; Ania, C.; Parra, J. B.; Cook, C. Dual Gas Analysis of Microporous Carbons Using 2D-NLDFT Heterogeneous Surface Model and Combined Adsorption Data of N2 and CO2. *Carbon* **2015**, *91*, 330–337. https://doi.org/10.1016/j.carbon.2015.05.004.
(37) Neimark, A. V.; Lin, Y.; Ravikovitch, P. I.; Thommes, M. Quenched Solid Density Functional Theory and Pore Size Analysis of Micro-Mesoporous Carbons. *Carbon* **2009**, *47* (7), 1617–1628. https://doi.org/10.1016/j.carbon.2009.01.050.
(38) Jagiello, J.; Olivier, J. P. 2D-NLDFT Adsorption Models for Carbon Slit-Shaped Pores with Surface Energetical Heterogeneity and Geometrical Corrugation. *Carbon* **2013**, *55*, 70–80. https://doi.org/10.1016/j.carbon.2012.12.011.
(39) Ravikovitch, P. I.; Vishnyakov, A.; Russo, R.; Neimark, A. V. Unified Approach to Pore Size Characterization of Microporous Carbonaceous Materials from N_2, Ar, and CO_2 Adsorption Isotherms. *Langmuir* **2000**, *16* (5), 2311–2320. https://doi.org/10.1021/la991011c.
(40) Jagiello, J. Stable Numerical Solution of the Adsorption Integral Equation Using Splines. *Langmuir* **1994**, *10* (8), 2778–2785. https://doi.org/10.1021/la00020a045.

(41) Jagiello, J.; Kenvin, J.; Celzard, A.; Fierro, V. Enhanced Resolution of Ultra Micropore Size Determination of Biochars and Activated Carbons by Dual Gas Analysis Using N2 and CO2 with 2D-NLDFT Adsorption Models. *Carbon* **2019**, *144*, 206–215. https://doi.org/10.1016/j.carbon.2018.12.028.

FOR TABLE OF CONTENTS ONLY